UNIVERSIDAD DE SONORA

DIVISIÓN DE CIENCIAS EXACTAS Y NATURALES
DEPARTAMENTO DE INVESTIGACIÓN EN FÍSICA

MEASUREMENTS OF THE LARGE HADRON COLLIDER LUMINOSITY USING THE CMS SILICON PIXEL DETECTOR

THESIS

in partial fulfillment of the requirements for the degree of:

Maestría en Ciencias (Física)

By:

Jesus Rodolfo MORENO CHAVEZ

Director:
Dr. Jose Feliciano BENITEZ RUBIO

Hermosillo, Sonora January 2023

Acknowledgements

I would like to thank my advisor Dr. José Feliciano Benítez Rubio for his guidance, patience and for giving me the opportunity to participate in the CMS collaboration. I would also like to thank my family and friends. And finally, acknowledgments to CONACYT for supporting my studies with financial aid.

Abstract

The calibration of the luminosity measurement from the analysis of the van der Meer scan program by the CMS experiment in the 2018 proton-proton data taking at $\sqrt{s}$ =13 TeV with the CMS Silicon Pixel detector is reported. The recorded data was reprocessed using a selection of the Pixel detector corresponding to the period from 2018-05-28 to 2018-07-07, based on luminosity stability studies. The background estimation corresponding to this module selection is reported. The analysis of the van der Meer scans presented here results in the calibration constant $\sigma_{vis} = 9229 \pm 8(\text{stat.}) \pm 28(\text{syst.})$ mb.

Resumen

Se reporta la calibración de la medición de luminosidad realizada a través del programa de escaneo de van der Meer del CMS en 2018 en la toma de datos protón-protón a $\sqrt{s}$ =13 TeV, para el detector de pixeles de silicio (Silicon Pixel detector). Los datos han sido reprocesados aplicando una selección de módulos del detector de pixeles que corresponde al periodo 28/05/2018 a 07/07/2018, basada en un estudio de estabilidad de luminosidad. La estimación del ruido de fondo en las mediciones correspondiente a esta selección de módulos es también reportada. El análisis de los escaneos de van der Meer presentados en este trabajo resulta en la constante de calibración $\sigma_{vis} = 9229 \pm 8(\text{stat.}) \pm 28(\text{syst.})$ mb.

Table of contents

List of figures

List of tables

Chapter 1

Introduction

Particle physics studies the fundamental constituents of the Universe, the elementary particles, and the interactions between them, the forces. To produce and study most of the elementary particles, experiments are carried out in particle colliders of high energy, where a wide range of technologies are employed to detect and measure the properties of the particles produced, and to measure the collider parameters for its perfomance.
This chapter gives a brief background of the elementary particles and particle colliders, as well as relevant concepts-definitions about the measurements studied in this thesis project.

1.1 Fundamental Particles

In our current understanding matter is made up of a group of particles with spin $1/2$, the fermions. The interactions between them, the forces, are described by the exchange of particles, which consist of a group of particles with integer spin: the gauge bosons. Three of the four forces: electromagnetic force, weak force and strong nuclear force, are mediated by the gauge bosons: photon, $W^{\pm}$ and Z^0, and gluons (g, eight of them), respectively. The description of the gravitational force in particle physics is yet an unresolved challenge. Apart from these vector bosons, there is a special scalar boson called Higgs boson, associated with the mechanism that give mass to all fundamental particles.
The group of fermions is categorized in two types: leptons and quarks, giving a total of twelve fundamental particles that compose the matter. There are six leptons, three charged: electron (e), muon (μ) and tau (τ), and their corresponding neutrinos: electron-neutrino (ν_e), muon-neutrino (ν_μ) and tau-neutrino (ν_τ). The other group of fermions are the quarks, which cannot be found as individual particles, they can only be found coupled forming particles called hadrons. The group of quarks is formed by the up quark (u), down quark

(d), charm quark (c), strange quark (s), top quark (t) and bottom quark (q) [1]. The force experienced by the fermions is shown in table 1.1.

Table 1.1 Force experienced by the fermions

				Electromagnetic	**Weak**	**Strong**
Leptons	e	μ	τ	✓	✓	
	ν_e	ν_μ	ν_τ		✓	
Quarks	u	c	t	✓	✓	✓
	d	s	b	✓	✓	✓

All these particles are described by the Standard Model (SM), so far the best theoretical model that provides a successful description of the experimental data. Most of the experimental data comes from particle colliders because most of the particles of the SM can only be produced and studied using collisions of high energy. One example of this, is the last member of the SM: the Higgs boson, observed in the Large Hadron Collider in proton-proton collisions at energy of 7 and 8 TeV in the CMS and ATLAS detectors [2, 3].

1.2 Particle Colliders

Particle physics experiments are designed to detect and identify the particles produced in high-energy collision. The colliding beams produce particle bunch interactions referred to as events.

Only the stable and relatively long-lived particles are the observables of particle physics collider experiments. The techniques employed to detect and identify the different particles depends on the nature of their interactions with matter. There are three main types of interactions (broadly speaking): interactions of charged particles, electromagnetic interactions of electrons and photons, and strong interactions of charged and neutral hadrons. The large particle physics detector systems use a wide range of technologies to detect and measure the properties of the particles produced in these high-energy collisions, with the aim of reconstructing the primary particles produced in the interaction from the signals in the different detector systems [4].

Apart from the technologies of detection, the most importar features for the performance of a particle collider are its center-of-mass (CM) energy and the luminosity. Achieving a high energy is required to collide particles and produce (possibly many) different particles. Some of them with considerably higher masses than the incident particles, for example massive particles such as the $W^{\pm}$, Z and H bosons. The total energy of a incoming particle plus the target particle depends on the reference frame. The frame that is relevant for

the production of high mass particles is the CM frame for which the incoming and target particle have equal and opposite momentum of magnitude p. Considering the Lorentz invariant quantity s :

$$s = (E_1 + E_2)^2 - (\mathbf{p}_1 + \mathbf{p}_2)^2 c^2$$

In the CM frame, where the momenta are equal and opposite, the second term vanishes so that

$$s = 4E^2$$

where E is the energy of each incoming particle and s is the square of the total incoming energy in the CM frame ;this is a quantity that appears often in particle physics and the notation $\sqrt{s}$ is always used to refer the CM energy. Using colliding beams of particle with equal mass having the same energy and therefore equal but opposite momentum, makes the experiment taking place in the CM frame and the full energy delivered by the accelerator, $\sqrt{s} = 2E$, can be used to produce high mass particles [5]. Colliding beam machines are used in particle physics experiments due the advantage of achieving much higher centre-of-mass energies in contrast with a fixed target experiment.
The other important parameter of a colllider, the luminosity $\mathscr{L}$, is the quantity that defines ability to produce large numbers of events [6]. It quantifies the potential of the collider for delivering a statistically significant sample of a given class of events. A high luminosity is of utmost importance in the search for rare events and new phenomena [7]. This quantity relates the event rates (number of events in time) and the cross section (σ_p) of a particular event; the cross section is a measure of quantum mechanical probability for the interaction.

1.3 Cross section

In order to illustrate the concept of cross section, we shall consider a simple case where a beam of particles of type a, with flux ϕ_a, is crossing a region of space in which there are n_b particles per unit volume of type b. The interaction rate per target particle r_b will be proportional to the incident particle flux, and can be written as [4]:

$$r_b = \sigma \phi_a$$

The fundamental physics is contained in σ, which has dimensions of area, and is termed as interaction cross section. There are cases where the cross section is closely related to the physical cross sectional area of the target, for example, neutron absorption by a nucleus. However, in general, the cross section is simply an expression of the underlying

quantum mechanical probability that an interaction will occur [4].
Fig. 1.1 (left) illustrates the definition of cross section, where a single incident particle of type a is travelling with a velocity v_a in a region defined by the area A, containing n_b particles of type$b$ per unit volume moving with a velocity v_b in the opposite direction to v_a.

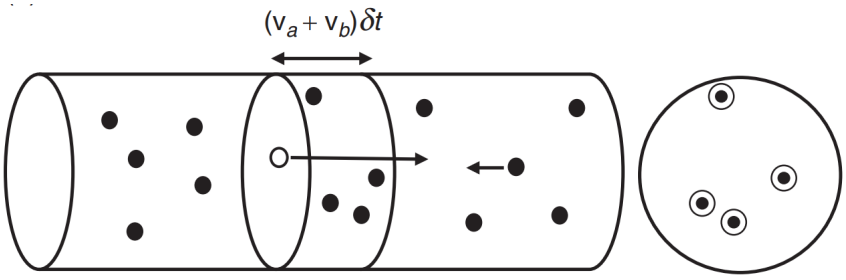

Fig. 1.1 Left: single incident particle of type a traversing a region containing particles of type b. Right: projected view of the region traversed by the incident particle in time δt [4].

For a time δt, the particle a crosses a region containing $\delta N = nb(v_a + v_b)A\delta t$ of type b. The interaction probability can be obtained from the effective total cross sectional area of the δN particles divided by the area A, which can be interpreted of as the probability that the incident particle passes through one of the regions of area σ drawn around each of the δN target particles, as shown in Fig. 1.1 (right) [4]. The interaction probability δP is therefore

$$\delta P = \frac{\delta N \sigma}{A} = n_b v \sigma \delta t \tag{1.1}$$

where $v = v_a + v_b$. The interaction rate for each particle of type a is

$$r_a = \frac{dP}{dt} = n_b v \sigma \tag{1.2}$$

For a beam of particles of type a with number density n_a confined to a volume V, the total interaction rate is

$$\text{rate} = r_a n_a V = (n_b v \sigma) n_a V = (n_a v)(n_b V)\sigma$$

$$\text{rate} = \phi N_b \sigma$$

so that the total rate is equal to

$$\text{rate} = \text{flux} \times \text{number of target particles} \times \text{cross section} \tag{1.3}$$

Thus, the cross section for a process is defined as

$$\sigma = \frac{\text{number of interaction per unit time per target particle}}{\text{incident flux}} \tag{1.4}$$

where the flux ϕ accounts for the relative motion of particles. One approach to calculate the cross section for a particular process can be using the relativistic formulation of Fermi's golden rule and the appropriate Lorentz-invariant expression for the particle flux.

The cross section for the production of a general final state O at the LHC is given by [8]:

$$\sigma(pp \to O+X) = \int dx_1 dx_2 \sum_{i,j} f_i(x_1,Q) f_j(x_2,Q) \hat{\sigma}(ij \to O)(M_O, g_{ijO}, \cdots) \tag{1.5}$$

where $f_i(x,Q)$ is the density fo partons[1] (PDF) of type i (quarks of different flavours or gluons) inside the proton, carrying a fraction x of the proton momentum at a resolution scale Q. Theory predicts the PDFs to be independent of O. $\hat{\sigma}(ij \to O)$ is the partonic cross section to produce the final state O in the collisions of partons i and j. It depends on properties of the final state (for example the mass of O, M_O, the momentum of the various particles involved, etc.), and on the the nature of the interactions involved in the process (for example the strength, g_{ijO}, of the coupling between i, j and O). Parameters like M_O and g_{ijO} are therefore what defines the underlying theory, and extracting their value as accurately as possible is the ultimate goal of an experimental measurement [8]. The precision of the extraction of these parameters is determined by [8]: i) The precision of the calculation of $\hat{\sigma}(ij \to O)$ as a function of M_O, g_{ijO}, etc.; this is a theoretical aspect. Inclusion of higher and higher orders of perturbation theory makes the prediction more accurate. ii) The precision of the knowledge of the PDFs; a theoretical and experimental aspect. For example, experimental data from measurements such as deep inelastic scattering (DIS) are necessary to extract the PDFs, by fitting these data to the DIS equivalent of an equation like 1.5. Likewise, is expected to use the LHC data themselves to improve the knowledge of the PDFs, by including the functions f_i to the list of parameters in eq. 1.5 that are allowed to float in order to fit the data.

[1] Before quarks and gluons were generally accepted, Feynman proposed that the proton was made up of point-like constituents, termed partons [4].

1.4 Luminosity

Luminosity, $\mathscr{L}$, is defined as the proportionality factor between the number of events per second R (event rates) and the cross section σ_p for a given process p [6]:

$$R = \mathscr{L}_{inst} \cdot \sigma_p \tag{1.6}$$

Cross section has units cm^2, therefore the unit of luminosity is $cm^{-2}s^{-1}$.
To derive a general expression of luminosity, we will consider the case of colliding beams at head-on. At head on collision, the instantaneous luminosity for N_b colliding bunches is given by:

$$\mathscr{L}_{inst} = N_b N_1 N_2 f \int_{-\infty}^{\infty} dx \int_{-\infty}^{\infty} dy \rho_1(x,y)\rho_2(x,y) \tag{1.7}$$

where $N_{1,2}$ are the particles per bunch, f the revolution frequency and $\rho_{1,2}$ are the distribution functions of the two beams in the transverse plane. Assuming that ρ can be factorized into independent terms in x and y, i.e. uncorrelated bunch densities in all planes:

$$\rho_i(x,y) = \rho_i(x)\rho_i(y) \qquad i = 1,2 \tag{1.8}$$

So that eq. 1.7

$$\mathscr{L}_{inst} = N_b N_1 N_2 f \int_{-\infty}^{\infty} \rho_1(x)\rho_2(x)dx \int_{-\infty}^{\infty} \rho_1(y)\rho_2(y)dy \tag{1.9}$$

If the bunch densities have Gaussian profile in both directions, i.e

$$\rho(u) = \frac{1}{\sqrt{2\pi}\sigma_u} exp\left(-\frac{u^2}{2\sigma_u^2}\right) \qquad u = x,y \tag{1.10}$$

The integration yields

$$\mathscr{L}_{inst} = \frac{N_1 N_2 N_b f}{4\pi\sigma_x\sigma_y} \tag{1.11}$$

In practice, the properties of the colliding beams are not know precisely, such as the bunch density profile, so that the integral in 1.9 cannot be solved analytically. In LHC a experimental technique is implemented with a dedicated machine setup to estimate the integrals, yielding a similar expression as 1.11. This is discussed in chapter 3.

The instantaneous luminosity measure is of great importance beacuse it reflects the performance of the collider, but this is not the only measurement concerned with luminosity. Another important measurement of luminosity is the integrated luminosity [6]:

$$\mathscr{L}_{int} = \int_0^T \mathscr{L}_{\text{inst}}(t)dt \tag{1.12}$$

The integral is taken over a period of time T (excluding possible dead time). The integrated luminosity has units of cm^{-2} and is often expressed in inverse barn ($1barn = 10^{-24}cm^2$). The importance of the integrated luminosity is because it directly relates to the number of observed events: $\mathscr{L}_{int} \cdot \sigma_p$.
Another important parameter for a beam with high luminosity and bunched beams are the number of particle collisions per bunch crossing, called pileup (μ). Pileup and luminosity are related by $f\mu = \mathscr{L}_{\text{inst}}\sigma_p$.
Up to date, the particle collider with the highest luminosity and energy is the Large Hadron Collider (LHC) built by CERN, located in Geneva, Switzerland.

1.5 Importance of Luminosity precision

The precision of the measured cross section, $\sigma_{exp}(O)$, is determined by the quantities on the right hand-side of: $\sigma_{exp}(O) = N_{\text{events}}(O)/\mathscr{L}_{int}$. N_{events} depends on the accurate knowledge of signal and background acceptances and efficiencies.
The target of the programme of precision measurements is therefore to bring to the same level the accuracy of all elements in the following relation:

$$\sigma(pp \to O) = \frac{N_{\text{events}}(O)}{\mathscr{L}_{int}}$$

The possibility to have a very accurate absolute luminosity determination, and therefore very accurate experimental cross section measurements, allows to develop a physics programme in which this precise information can help improve, at the same time, the theoretical calculations, the PDF knowledge, and ultimately the measurement of the theory parameters such as masses and couplings[8]. The experimental techniques to determine signal rates are mature enough, where the understanding of acceptances, detector biases, reconstruction efficiencies or background subtraction is at the subpercent level, so that the final precision of the physics measurement is dominated by the luminosity uncertainty [7]. The precision in the measurement of the luminosity directly impacts the precision in the measurement of the cross section, and therefore has a large impact in our understanding of the Standard Model parameters.

1.6 The Large Hadron Collider

The LHC was designed to collide proton beams with a centre-of-mass energy of 14 TeV and a luminosity of $10^{34} cm^{-2} s^{-1}$. It was also designed to collide heavy (Pb) ions with an energy of 2.8 TeV per nucleon and a peak luminosity of $10^{27} cm^{-2} s^{-1}$ [9].
The LHC consists of two rings of 27 km of circumference which guide accelerated bunches of protons (or Pb) at high energy to collide. Figure 1.2 shows the CERN accelerator complex. The bunches are previously accelerated by a chain of pre-accelerators. First, protons are produced by ionizing hydrogen and then are transferred to the Linear Accelerator 2 (LINAC2) where the protons are accelerated in bunches up to an energy of 50 MeV, and then the bunches pass trough three circular accelerator: the Booster, the Proton Synchrotron (PS) and the Super Proton Synchrotron (SPS), giving an energy of 1.4 GeV, 26GeV and 450 GeV, respecectively. After these three preaccelerators, the bunches are finally circulating in oposite directions in the LHC ring, where are further accelerated to reach energies up to 7 TeV (per bunch). This entire procedure defines a single LHC fill generally consisting of 10^{14} protons, grouped into bunches to form the proton beam.
There are four experiments placed around the LHC ring: Compact Muon Solenoid (CMS) [10], A Toroidal LHC ApparatuS (ATLAS) [11], A large Ion Colliding Experiment (ALICE) [12] and LHCb [13]. CMS and ATLAS are for general-purpose detectors to investigate the largest range of SM and Beyond SM (BSM) physics. ALICE and LHCb have detectors specialized to study specific phenomena.

1.7 LHC Luminosity

The LHC has had two Runs and two long shutdowns for maintenance and upgrades. Run 1 lasted from 2010-2012, while Run 2 lasted from 2015-2018. In Run1, LHC reached a peak instantaneous luminosity of 0.77×10^{34} and an integrated luminosity of $25 fb^{-1}$ for proton-proton collisions at $\sqrt{s} = 8$ TeV in 2012[15]. For the first part of Run-2 (2015-2016) in proton-proton colissions at $\sqrt{s} = 13$TeV in CMS detector, the integrated luminosities when CMS was fully operational are 2.27 and 36.3 fb^{-1} in 2015 and 2016, with a relative precision of 1.6% and 1.2%, respectively [16]. For the second part of Run 2 (2017-2018), the integrated luminosity is about $49.8 fb^{-1}$ and $67.9 fb^{-1}$ for 2017 and 2018, respectively, as can be seen in Fig. 1.3. The total systematic uncertainty in the calibration of luminosity measurement is 2.3% in 2017[17] and 2.5% in 2018 [18], but its precision remains to be improved. The main objective of this thesis project is to contribute to the improvement of the precision of 2018 luminosity calibration.

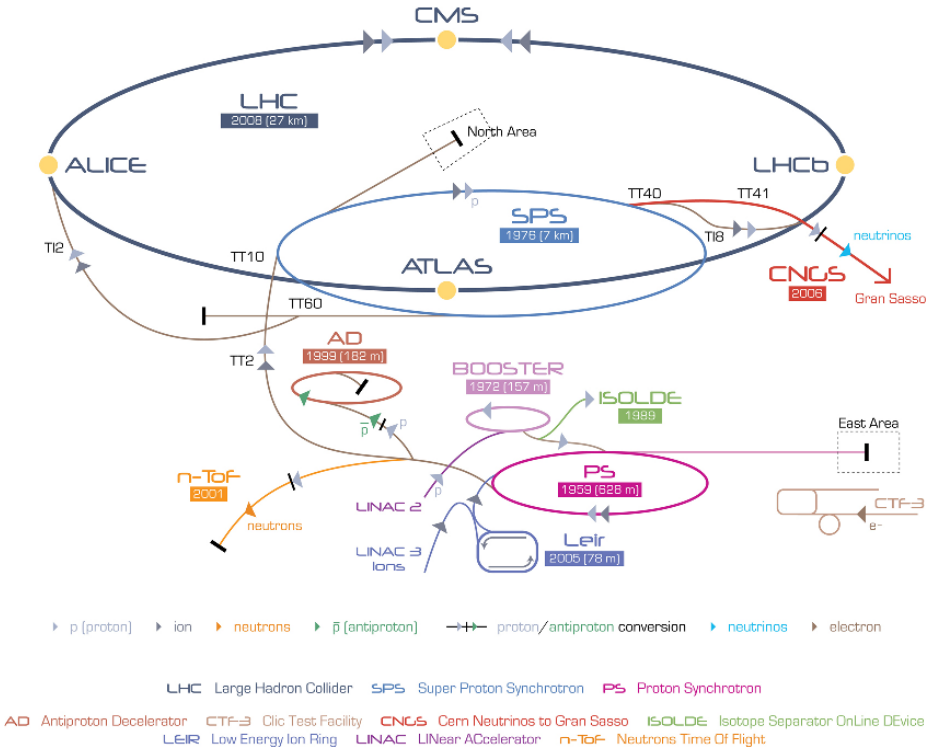

Fig. 1.2 Diagram of the LCH complex [14].

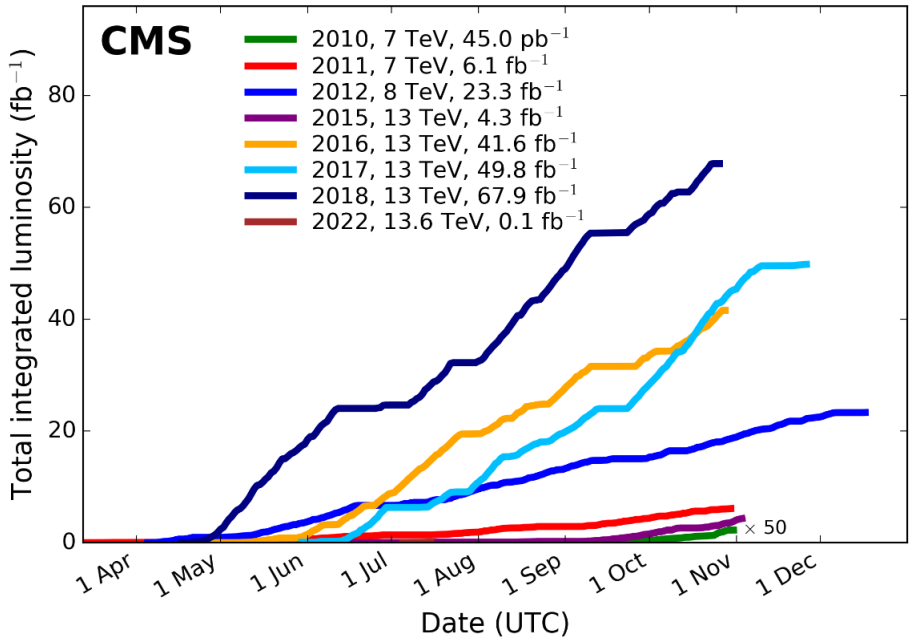

Fig. 1.3 Delivered luminosity versus time for Run-1 (2010-2012) and Run-2 (2015-2018); pp data only. Cumulative luminosity versus day delivered to CMS during stable beams for pp collisions at nominal center-of-mass energy. These plots use the best available offline calibrations for each year. For 2017 and 2018 the plots are based on [17] and [18], respectively [19].

Chapter 2

Experiment Description

The Compact Muon Solenoid (CMS) detector is a multi-purpose apparatus that operates at the LHC at CERN. Its name comes from the fact that is quite compact for all the detector material it contains (15 meters high and 21 meters long), it is designed to detect muons very accurately, and it has it has the most powerful solenoid magnet ever made. Along with ATLAS, is one of the two high luminosity experiments at CERN. In this chaper the components of the CMS are described. The silicon pixel tracker is described with more detail due the purposes of this thesis.

2.1 The Compact Muon Solenoid

The Compact Muon Solenoid (CMS) experiment is one of four detectors placed around the LHC. The CMS detector consist of several detection layers, having a total length of 21.6 m with a diameter of 14.6 m. It consist of a silicon tracker to provide a measurement of the trajectories of charged particles, a 3.8 Tesla superconducting solenoid, an electronic and hadronic calorimeter to meausure particle energy, and a muon detection system [10]. A diagram of a perspective view of the CMS detector is shown in Fig. 2.1.
The electromagnetic calorimeter of CMS (ECAL) is a hermetic homogeneous calorimeter made of 61 200 lead tungstate (PbWO4) crystals mounted in the central barrel part, closed by 7 324 crystals in each of the two endcaps. A preshower detector is placed in front of the endcap crystals. Avalanche photodiodes (APDs) are used as photodetectors in the barrel and vacuum phototriodes (VPTs) in the endcaps [10].
The ECAL is surrounded by a brass/scintillator sampling hadron calorimeter (HCAL). The scintillation light is converted by wavelength-shifting (WLS) fibres embedded in the scintillator tiles and channeled to photodetectors via clear fibres. This light is detected by photodetectors (hybrid photodiodes, or HPDs) that can provide gain and operate in

high axial magnetic fields. The Cerenkov light emitted in the quartz fibres is detected by photomultipliers [10].
After the HCAL and the 13-m-long, 6-m-inner-diameter, 4-T superconducting solenoid, the muon detector system is placed. CMS uses 3 types of gaseous particle detectors for muon identification. Due to the shape of the solenoid magnet, the muon system was naturally driven to have a cylindrical, barrel section and 2 planar endcap regions [10].
The tracker system is described with detail in the next section.
A sketch of a transverse slice of the CMS detector, with specific particle interactions, is shown in Fig. 2.2. A simplified summary of particle interaction (and detection) is described as follows. Starting from the beam interaction region, particles first enter a tracker, in which charged-particle trajectories (tracks) and origins (vertices) are reconstructed from signals (hits) in the sensitive layers. The tracker is immersed in a magnetic field that bends the trajectories and allows the electric charges and momenta of charged particles to be measured. Electrons and photons are then absorbed in an electromagnetic calorimeter (ECAL). The corresponding electromagnetic showers are detected as clusters of energy recorded in neighbouring cells, from which the energy and direction of the particles can be determined. Charged and neutral hadrons may initiate a hadronic shower in the ECAL as well, which is subsequently absorbed in the hadron calorimeter (HCAL). Muons and neutrinos traverse the calorimeters with little or no interactions. While neutrinos escape undetected, muons produce hits in additional tracking layers called muon system, located outside the calorimeters [20].

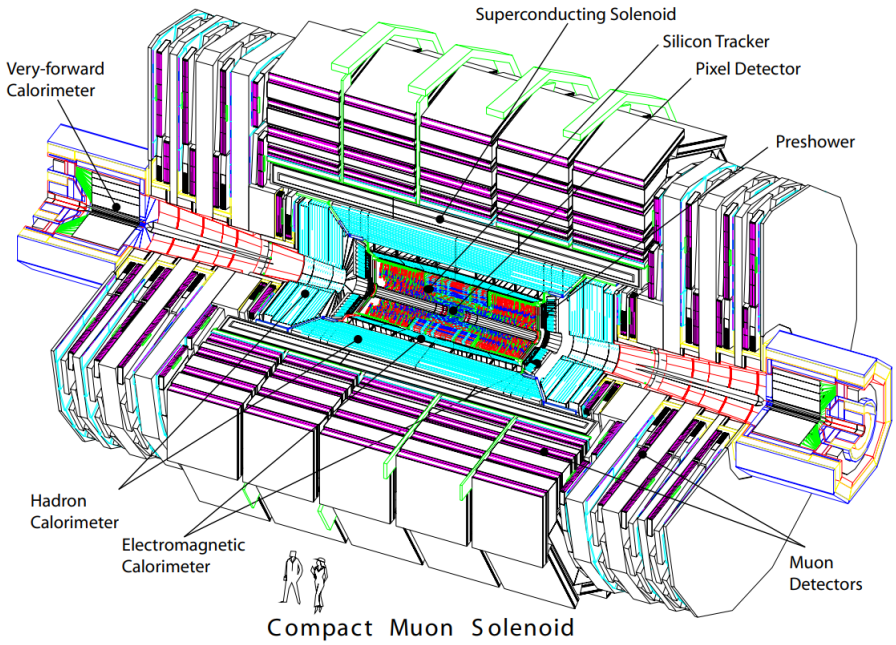

Fig. 2.1 Perspective view of the CMS detector.

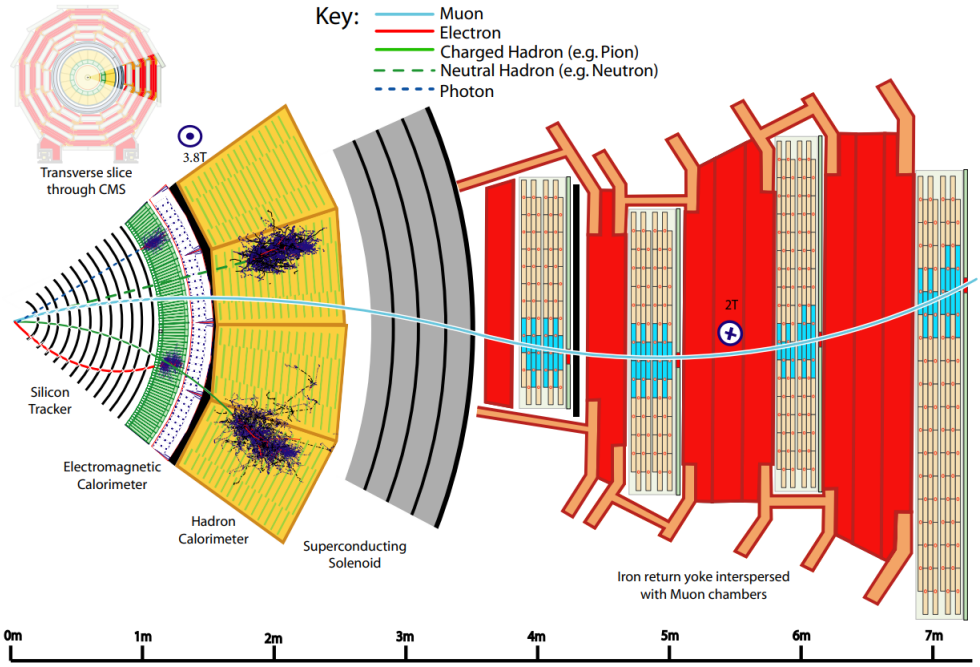

Fig. 2.2 Sketch of a transverse slice of the CMS detector with specific particle interactions, from the beam interaction region to the muon detector. The muon and the charged pion are positively charged, and the electron is negatively charged [20].

The coordinate system adopted by CMS has the origin at the center of the detector, the y-axis pointing vertically upward, and the x-axis pointing radially inward toward the center of the LHC. Thus, the z-axis points along the beam direction toward the Jura mountains from LHC Point 5. The azimuthal angle φ is measured from the x-axis in the $x-y$ plane and the radial coordinate in this plane is denoted by r. The polar angle θ is measured from the z-axis. Pseudorapidity is defined as $\eta = -\ln\tan(\theta/2)$ [10].

2.2 CMS Tracking System

The measurement of the momenta of charged particles is an essential aspect of any large particle physics experiment. Regardless of the medium through which a charged particle travels, it leaves a trail of ionised atoms and liberated electrons. By detecting this ionisation it is possible to reconstruct the trajectory of a charged particle. A charged particle will leave a hit in a silicon sensor in each cylindrical layer from which the trajectory of the

charged particle track can be reconstructed.[4].
When a charged particle passes through a medium, it interacts electromagnetically with the atomic electrons and loses energy through the ionisation of the atoms [4]. The theory of such losses, which are due dominantly to Coulomb scattering from the atomic electrons, was worked out by Bethe, Bloch and others in the 1930s. The result is called the Bethe–Bloch formula: [21]:

$$-\frac{dE}{dx} = \frac{Dq^2 n_e}{\beta^2}\left[\ln\left(\frac{2m_e c^2\gamma^2}{I}\right) - \beta^2 - \frac{\delta(\gamma)}{2}\right] \tag{2.1}$$

x is the distance travelled through the medium, m_e is the electron mass, $\beta = v/c$, $\gamma = (1-\beta^2)^{-1/2}$ and $D = \frac{4\pi\alpha^2\hbar^2}{m_e}$ =5.1×10^{-25}MeV cm^2. The other constants refers to the medium: n_e is the electron density, I is the mean ionisation potencial of the atoms averaged over all electrons (given approximately by I=10ZeV for Z >20) and δ is a dielectric screening correction that is only important for highly relativistic particles.

The tracking detector in the CMS experiment is based on semiconductor technology using silicon pixels and strips. It is composed of two sub systems, the pixel tracker (the closest to the interaction vertex) and the strip tracker [10]. The Pixel detector is described below.

2.2.1 Pixel Detector and Clustering

The pixel tracker originally consisted of three barrel layers at radii of 44, 73, and 102 mm and two endcap disks on each end [10]. With the upgrade of the accelerators during the first long shutdown (LS1, 2013-2014) the original pixel detector has been replaced by a new system referred to as the CMS Phase-1 pixel detector. The installation of the CMS Phase-1 pixel detector took place during the extended year-end technical stop of the LHC in 2016/2017. The layout of the CMS Phase-1 pixel detector is optimized to have four-hit coverage over the pseudorapidity range ($|\eta| < 2.5$), improved pattern recognition and track reconstruction, and added redundancy to cope with hit losses [22].
The CMS Phase-1 pixel detector consists of four concentric barrel layers (L1-L4) at radii of 29, 68, 109, and 160 mm, and three disks (D1-D3) on each end at distances of 291, 396, and 516 mm from the center of the detector. The layout of the CMS Phase-1 pixel detector is shown in Fig. 2.3. The total silicon area of the CMS Phase-1 pixel detector is 1.9 m^2, while the total silicon area of the original pixel detector was 1.1 m^2.

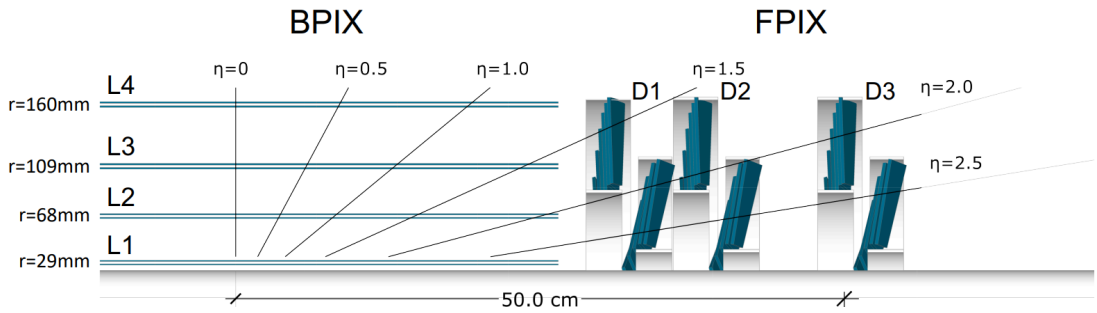

Fig. 2.3 Layout of the CMS Phase-1 pixel detector in longitudinal view[22].

The CMS Phase-1 pixel detector is built from 1856 segmented silicon sensor modules, where 1184 modules are used in the barrel pixel detector (BPIX) and 672 modules are used for the forward disks (FPIX). Each module consists of a sensor with 160×416 pixels connected to 16 readout chips (ROCs). In total there are 124 million readout channels [22]. The CMS Phase-1 pixel detector uses a similar module design as the BPIX modules of the original detector. A pixel detector module is built from a planar silicon sensor with a size of 18.6 × 66.6 mm^2 (active area of 16.2 × 64.8 mm^2), bump-bonded to an array of 2×8 ROCs. Each ROC is segmented into 4160 readout channels and reads out the pulse height information for each pixel. The standard pixel size is 100×150 μm^2, as in the original pixel detector.Drawings of the CMS Phase-1 pixel detector modules are shown in Fig. 2.4 [22].

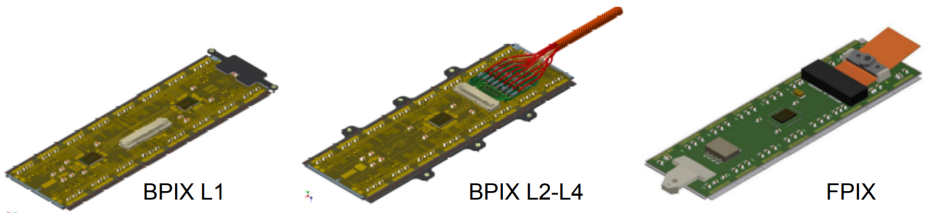

Fig. 2.4 Drawings of the pixel detector modules for BPIX L1 (left), BPIX L2–4 (middle), and the FPIX detector (right)[22].

In the BPIX detector, the orientation of the sensor surface of the modules is parallel to the magnetic field. The pixels are oriented with the long side parallel to the beam line. In the FPIX detector, the modules in the outer rings are rotated by 20° in a turbine-like geometry. However, to obtain optimal resolution in both the azimuthal and radial directions for the inner ring, the modules in the inner ring are arranged in an inverted cone array tilted by 12° with respect to the beam line, combined with the 20° rotation. The sensor orientation in the FPIX detector is such that the long side of the pixel is in the radial direction [22].

The sensors of the BPIX and FPIX detectors were produced by different companies in order not to depend on a single source. The concept and design were tailored to each vendor's production process, leading to two different sensor types. Both types of sensors are made of silicon and follow the n-in-n approach, with strongly n-doped (n+) pixelated implants on an n-doped silicon bulk and a p-doped back side. In a reverse-bias configuration, the n+ implants collect electrons [22].
A Photograph of four pixel cells on a BPIX sensor and schematic of two pixel cells on an FPIX sensor is shown in Fig. 2.5.

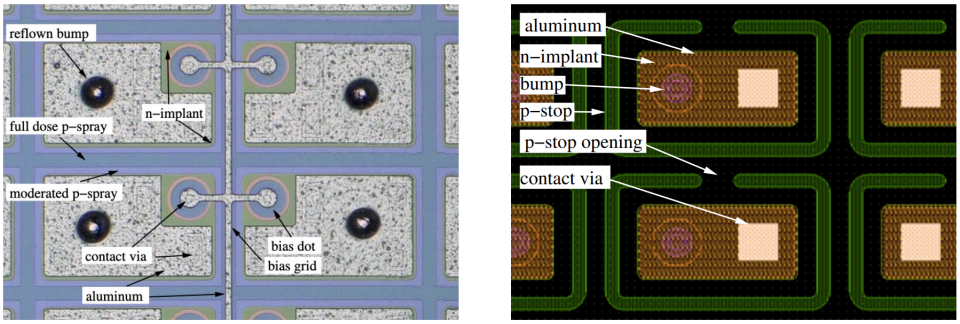

Fig. 2.5 Photograph of four pixel cells on a BPIX -sensor (left) and schematic of two pixel cells on an FPIX sensor (right) [22].

The most probable value of energy deposition for normally incident minimum-ionizing particles (MIPs) in a silicon sensor with a thickness of 285 μm corresponds to approximately 21000 electrons. This charge is frequently spread over more than one pixel due to Lorentz drift and diffusion of collected electrons, leading to charge clusters. In the track reconstruction step, hit pixels are combined to form clusters from neighboring pixels. The charge measured within the cluster corresponds to the charge deposited by a single charged particle [22].
The rest of the tracker system surrounds the Pixel detector: the Strip tracker, as can be seen in Fig. 2.6. It is composed of for subsystems: the Tracker Inner Barrel (TIB) and Disks (TID), the Tracker Outer Barrel (TOB) and The Tracker EndCaps (TEC). TIB and TID are composed of four barrel layers, supplemented by three disks at each end; TOB consists of six barrel layers; Each TEC is composed of nine disks, containing up to seven concentric rings of silicon strip modules. The strip tracker has in total 15 148 silicon modules, which cover an active area of about 198m^2 and have 9.3 million strips [10].

The first step of the track reconstruction process is referred to as local reconstruction. It consists of the clustering of zero-suppressed signals above specified thresholds in pixel

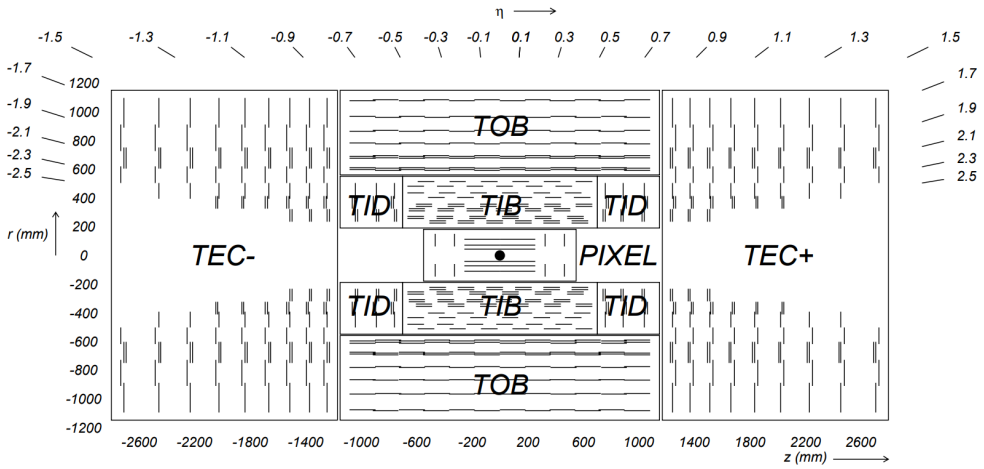

Fig. 2.6 Schematic cross section through the CMS tracker. Each line represents a detector module [10]. The Pixel tracker here is not the CMS Phase-1 pixel detector.

channels into hits, and then estimating the cluster positions and their uncertainties defined in a local orthogonal coordinate system (u,v) in the plane of each sensor. The pixel sensor consists of $100 \times 150 \mu m^2$ pixels with the u-axis oriented parallel to the shorter pixel edge. Offline, pixel clusters are formed from adjacent pixels, including both side-by-side and corner-by corner adjacent cells. Each cluster must have a minimum charge equivalent to 4000 electrons [23].

2.2.2 CMS Luminometers

Various systems are used for measuring luminosity at CMS. The Pixel Luminosity Telescope (PLT) and Fast Beam Conditions Monitor (BCM1F) are dedicated systems for luminosity measurement, while the hadronic forward calorimeter (HF) uses a dedicated readout on an existing system; these three use a separate data acquisition (DAQ) system, BRILDAQ, which operates independently of the main CMS readout [18].
The PLT uses silicon pixel sensors arranged into 16 “telescopes”, each having three sensor planes arranged nearly parallel to the beam pipe, where the rate of “triple coincidences” is measured; a hit is observed in all three planes.
BCM1F consists of a total of 24 sensors mounted on the same carriage as the PLT, consisting of a total of 10 silicon sensors, 10 polycrystalline diamond (pCVD) sensors, and 4 single-crystal diamond (sCVD) sensors.
The HF luminosity measurement uses a dedicated readout system installed in the HF calorimeter. Only two HF rings are used for luminosity measurement, to ensure relatively uniform occupancy. Two algorithms are available: the first relies on the fraction of occupied towers (HFOC), and the second is based on the sum of the transverse energy ET (HFET).

In addition other methods that uses data from existing parts of the CMS detector performs a luminosity measurement using the main CMS DAQ system. One of them is the drift tube luminosity (DT) which uses the rate of muon track stubs in the muon barrel track finder. Also, the RAMSES detectors, a CERN radiation and environmental monitoring sytem, although not being designed as a luminometer does function quite well as a luminosity measurement; it uses the rate observed in the detectors (primarily photons within the energy range of 50 keV to 7 MeV).
Other method is the pixel cluster counting (PCC), which will be described with more detail in chapter 3.

Chapter 3

Luminosity Measurement and Calibration

The precision measurement of the luminosity delivered to the CMS by the LHC is important for a variety of reasons. Online, the luminosity measurement provides realtime feedback on the LHC performance and operation. Offline, the luminosity measurement is a crucial component of physics analysis, either for measuring the cross section of observed processes or for setting upper limits in searches for processes BSM [18].
A total of seven systems are used for measuring luminosity at CMS. These systems are referred to as luminometers. Each luminometer reads out a rate of the specific quantities observed in the detector (hits, tracks, clusters, etc.). This rate, R, should be proportional to the instantaneous luminosity,$\mathscr{L}_{inst}$, with the constant of proportionality given by the visible cross section σ_{vis} [18]:

$$R = \mathscr{L}_{inst}\sigma_{vis} \tag{3.1}$$

The determination of σ_{vis} is carried out through van der Meer (vdM) scans performed with a dedicated LHC machine setup, exploited by S. Van der Meer for luminosity measurements at ISR [24].

3.1 Pixel Cluster Counting method

The Pixel Cluster Counting method exploits the very large number of pixels in the tracker of the CMS detector. At design luminosity of $10^{34}cm^{-2}s^{-1}$, the detector occupancy is less than 0.1% on average (the average number of clusters per minimum bias interaction is about 50 and the average number of pixels per cluster is about 5) [25]. The very low

occupancy leads to an excellent linear detector response with increasing LHC luminosity [18].
The PCC method uses the rate of pixel clusters in the CMS pixel detector to provide an offline luminosity measurement. Pixel clusters are formed from adjacent pixels, as mentioned in section 2.2.1. PCC measurement uses the data collected with the standard CMS trigger system with triggers requiring colliding bunches but not any specific event activity; this is referred as "zero-bias trigger" [18].
Each bunch crossing gives rise to some number of pp interactions, with each such interaction resulting in some number of pixel clusters. If the average over several zero-bias events is taken, the mean number of pixel clusters per event is [26]:

$$\langle N_{\text{cluster}} \rangle = \langle N_{\text{pixel/interaction}} \rangle \langle N_{\text{interactions}} \rangle \equiv \langle N_{\text{pixel/interaction}} \rangle \mu \tag{3.2}$$

where in the last step, the average number of interactions per bunch crossing, pileup, is denoted by the symbol μ.

3.2 Luminosity calibration: van der Meer method

In the practice, as mentioned in chapter 1, the properties of the colliding beams are not know precisely, such as the bunch density profile, so that the integral in 1.9 cannot be solved analytically. In LHC a experimental techinque know as vdM method is implemented with a dedicated machine setup to bring the bunch density profiles close to Guassian distributions. The VdM scan method, applied by LHC Experiments in Run 1 and Run 2, allows to measure and evaluate the integral over the proton bunch densities in eq. 1.9. For the vdM scan method to be applicable it is also assumed that the two bunch ρ can be factorized into independent terms in x and y [27]. The value of the two beam overlap integrals in Eq. (2) is determined by varying the beam separation and measuring the resulting rates [18]:

$$\int \rho_{x1}(x)\rho_{x2}(x)dx = \frac{R_x(0)}{\int R_x(\Delta)d\Delta} \tag{3.3}$$

where $R_x(\Delta)$ is the rate measured when the two beams are separated in x by a distance Δ; a asimilar equation can be written in y. Then the beam overlap width Σ_x (and similarly Σ_y) is defined as [18]:

$$\Sigma_x = \frac{1}{\sqrt{2\pi}} \frac{\int R_x(\Delta)d\Delta}{R_x(0)} \tag{3.4}$$

yielding the final expression for luminosity (for one single bunch):

$$\mathscr{L}_{inst} = \frac{N_1 N_2 f}{2\pi \Sigma_x \Sigma_y} \tag{3.5}$$

where $N_{1,2}$ are the particles per bunch (bunch current) and $f = 11246$ Hz is the bunch orbit frequency around the LHC ring.
This expression can be finally used in 3.1 to get σ_{vis}:

$$\sigma_{vis} = \frac{2\pi \Sigma_x \Sigma_y R(0,0)}{N_1 N_2 f} \tag{3.6}$$

Experimentally, two separate scans in the x and y directions are performed. The beams are scanned against each other while measuring the rate (normalized by the product of the beam currents) at a certain number of separation steps, fitting the resulting points with a functional form, and using the fitted function to extract $\Sigma_{x,y}$ and $R(0,0)$ in 3.6. Fig. 3.1 shows an sketch of the beam positions during vdM scans in X and Y planes together with the detector rate as a function of beam separation.

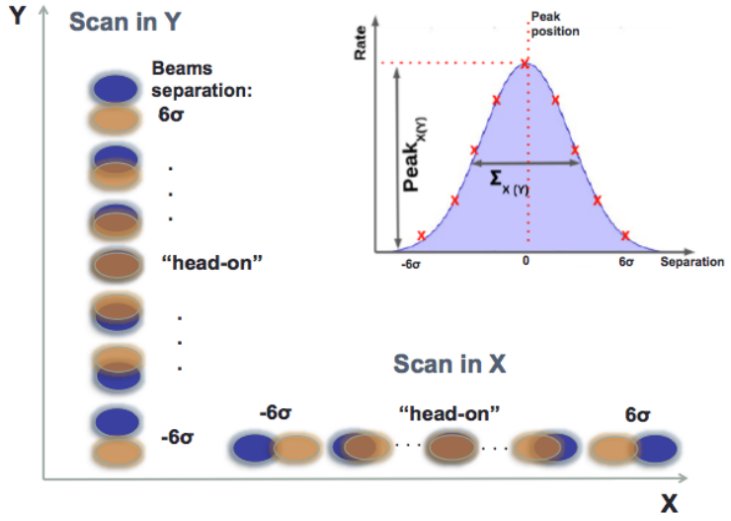

Fig. 3.1 The sketch of a vdM scan in X and Y planes. The indent sketch is an example of the fitting of the resulting rates [28].

Backgrounds

Before performing the fit to extract Σ_x and Σ_y, the raw measured rates must be corrected for background in the detector. The background contribution is estimated independently, using a special period known as Super Separation period where the beams are separated, ensuring that the only contribution is from background either beam-induced background or detector

noise. There are three sources of beam-induced background: Beam Gas Elastic (BGE), Beam Gas Inelastic (BGI) and Beam Halo (BH). BGE contribution are all coherent and quasi-elastic nuclear elastic and coulomb scattering for multi-turn beam-gas interactions around the ring; typically the interaction of the primary beam proton and the aperture takes place at the collimator. BGI are all inelastic interactions of primary beam protons with rest gas in the beam pipe. The interaction rate is dominated by the vacuum quality in the various beam line elements upstream CMS; therefore the origin of this contribution is distributed all along the long straight section. BH component is caused by the inefficiency of the main collimation system. Protons can escape from one collimator and being intercepted by another collimator [29].
Several other corrections are applied to the raw data before the vdM fit is performed.

Chapter 4

Analysis and Results

4.1 2018 vdM scan program

For 2018, the vdM scans were performed during LHC fill 6868 on June 30 and July 1 at pp collision energy $\sqrt{s}$ of 13 TeV. The LHC filling scheme used 124 colliding bunch pairs at the CMS interaction point (IP5) widely spread over the orbit to reduce long-range beam-beam effects and detector afterglow. The resulting beam size σ_b at the beginning of the fill was in the range of approximately 85–95 μm and 80–90 μm in x and y, respectively, increasing over time in the x dimension and decreasing over time in the y dimension. No crossing angle was used for collisions. The resulting peak pileup was approximately μ = 0.6, much lower than in a regular physics fill ($< \mu >= 32$ in 2018) [18].
The bunch intensities were approximately 7–9$\times 10^{10}$ protons per filled bunch, resulting in a total beam intensity of slightly above 10^{13} protons per beam. The total beam intensities were measured with the DC Current Transformers (DCCT), and the bunch currents were measured with the Fast Beam Current Transformers (FBCT) [18].
To ensure a dataset with a high event count for PCC even at large beam separations, CMS gated the zero-bias triggers on 5 bunch pairs: BCIDs (Bunch Crossing ID) 265, 865, 1780, 2192, and 3380; and recorded events with a total rate of 27.7 kHz [18].
The CMS vdM scan program was conducted in two parts due to an alarm. Apart from the vdM scans other studies were carried out called Imaging Scans, which can also be used to measure σ_{vis}. Imaging scans are performed by moving only one beam. The standard vdM scans are referred as “norm” and the imaging scans as “img”. In the first part of the scan program a vdM scan “norm1” and a imaging scan “img1” were carried out. The second part consisted of the scans “img2”, “img3”, “norm2”, “norm3” and “norm4” were done. In total are 7 scans to determine σ_{vis} [18].
In the vdM scans the two beams were separated by $6\sigma_b \approx 600\mu$m and scanned across

one another in a sequence of 25 steps with 30 seconds per step. For the beam imaging scans one beam (beam 1 in the first pair, followed by beam 2 in the second pair) is kept fixed at its nominal position while the other is separated and scanned in 19 steps from $+4.5\sigma_b$ to $-4.5\sigma_b$ with 46 seconds per step. In each of both scans (scan pairs), the scan was performed first in the x direction and then in the y direction.

For the background estimation, two Super Separation (SS) periods were carried out during the scan program, each 5 minutes long where the beams were separated by $6\sigma_b$ (where σ_b the beam size) in both the x and y directions; the first SS period took place after norm3 and the second after norm4.

Fig. 4.1 shows the beam positions for the two beams in the x and y directions as measured by the DOROS BPMs during the scan program, showing all scan pairs of the 2018 scan program.

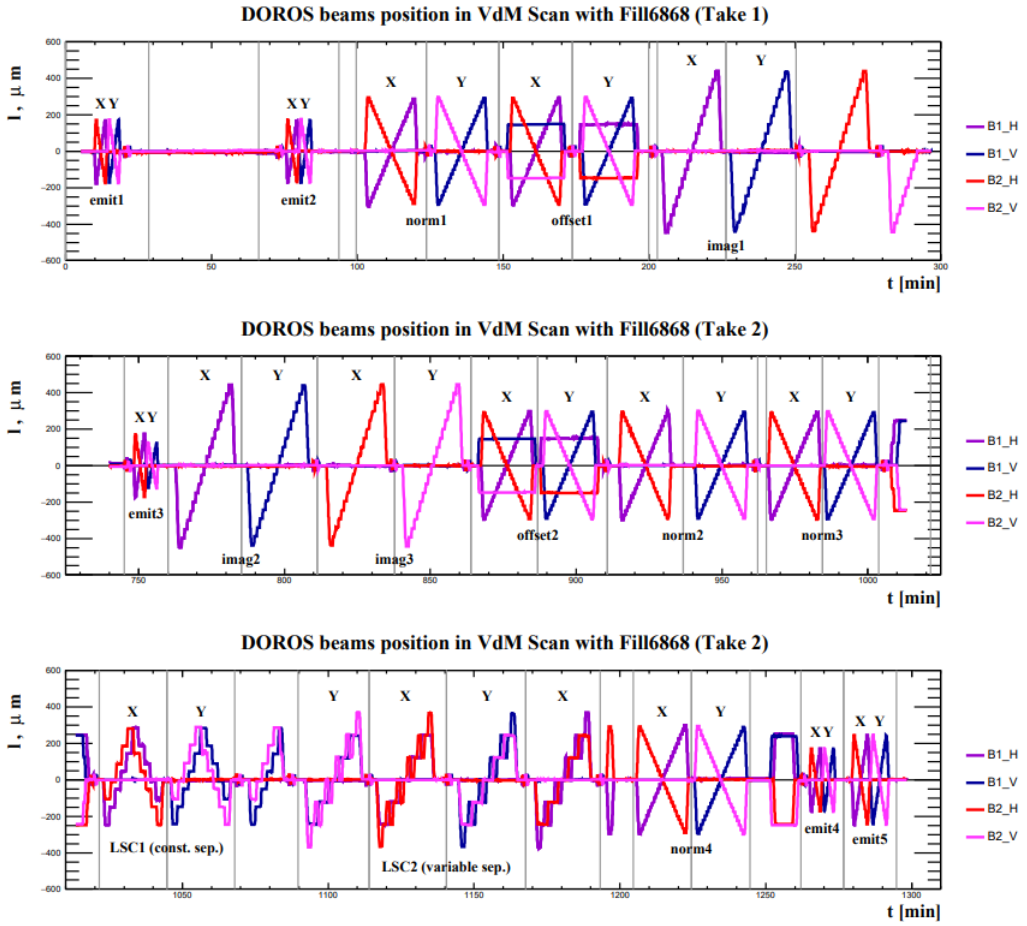

Fig. 4.1 Relative change in beam positions measured by the DOROS BPMs during the 2018 scan program for the two individual beams in the horizontal x and vertical y planes, as a function of the elapsed time from the beginning of the program. The top row shows the take 1 of the program before the alarm at CMS, while the bottom two rows show the program after the alarm [18].

4.2 Data analysis

The data recorded was processed with the CMS software (CMSSW) storing the data into a Hierarchical Data Format (HDF) with hd5 format, containing the times, beam positions, beam currents, and rates.
The data collected during the vdM scans is analysed with a software framework called "vdM Framework" (vdM FW), which is written in Python2 and uses the CERN's data analysis package "ROOT" trough the "PyRoot" library. With the analysis and plotting tools, the vdM FW reads the hd5 file, producing some intermediate files: scan file, beam currents file, rates file and correction files, and applies some corrections to rates (Background, DynamicBeta), separation (OrbitDrift, LengthScale, BeamBeam) and beam currents (FBCT to DCCT calibration, Ghost and Satellite) and creates a graph file. This graph file contains the normalized rates (i.e. R/N_1N_2) and beam position. Each point correspond to the averaged rates in a time window of 30s and 46s for vdM scans (norm) and imaging scans, respectively. The points are then fitted with a predefined function to extract $\Sigma_{x,y}$ and peak values to compute σ_{vis} for all the bunches in the scan.

For some luminometers the rates are reprocessed, for example for backround subtracting. In the case of PCC the data was reprocessed for two purposes: i) the use of new data format and ii) a different selection of the pixel detector modules.
For PCC, the rates (and the corresponding times) were originally stored per event into a ROOT file. Due the vdM FW procedures, the data analysis with the ROOT file carries some limitations, leading to the use of only 1% of the statistics. For this reason, the PCC data was reprocessed to store the data into an hd5 files containing the rates stored per 1.32 s (NB4), allowing the use of the full statistics. This leads to a large improvement in the statistical uncertainty in the rates by a factor of 10, improved the fit model and the better determination of the beam parameters, relative to the previous analysis reported in ref. [18].

4.3 Module selection

The implementation of a different selection of the modules in the pixel detector aims to remove instabilities in luminosity measurement. Previously, the same selection of modules was used for most of the year, for many run periods. Run periods corresponds to a division of time periods of the data set, for 2018 the calibration period is contained in the run period

2018-05-28 to 2018-07-07.
Using a different selection of modules per run period is more realistic as each period can have different number of good performing modules. The pixel detector conditions change over the time, for example by detector noise, aging effects and radiaiton damage.
The selection is done trough a module stability study. Module stability is based on variation of cluster count relative to total cluster count (module weight), root mean square (RMS) of weights distribution. The variations are considered in an interval of 23s (lumi section), which corresponds to the granularity (that is, the scale or level of detail in a set of data) of the luminosity database. Modules in barrel layer 1 are removed as these modules were not used in luminosity measurement. The module stability is re-evaluated (RMS values, 4% RMS selection) by using iterative process until stable luminosity is attained. Fig. 4.2 shows an example of a good and bad module.
For the calibration period, the module selection provided has 802 bad modules and 1054 good modules.
The results obtained from the analysis with the new selection of modules are shown below.

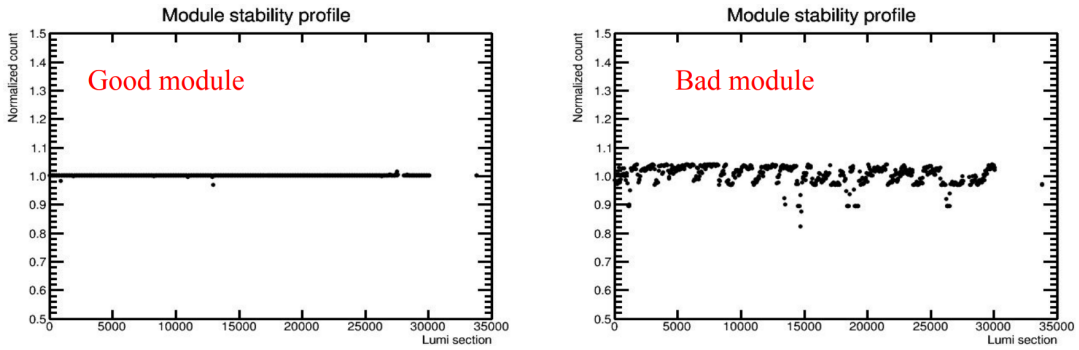

Fig. 4.2 Graphs showing stability profile for good and bad modules where weight is plotted as a function of lumi section.

4.4 Background estimation

To estimate the constant term in the measurements two super separation periods were carried out. Fig 4.3 shows PCC per NB4 versus time for BCID 1780 to illustrate the two SS periods. The lower regions corresponds to the time window of 5 min where the beams were separate a distance of $6\sigma_b$, ensuring thatensuring that the only contribution is from background (either beam-induced background or electronics noise). The background value in each BCID is estimated as the mean value of the distribution (or profile) of PCC per NB4. Fig 4.4 shows the distribution of PCC per NB4 for BCID 1780 for SS period I, having a mean value of 0.322 with a standard error of the mean (SEM) of 0.018.

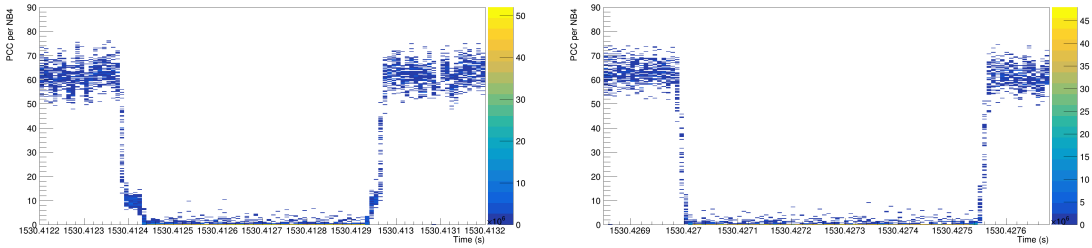

Fig. 4.3 PCC per NB4 versus time for BCID 1780. The lower regions corresponds to the super separation period I (left) and II (right).

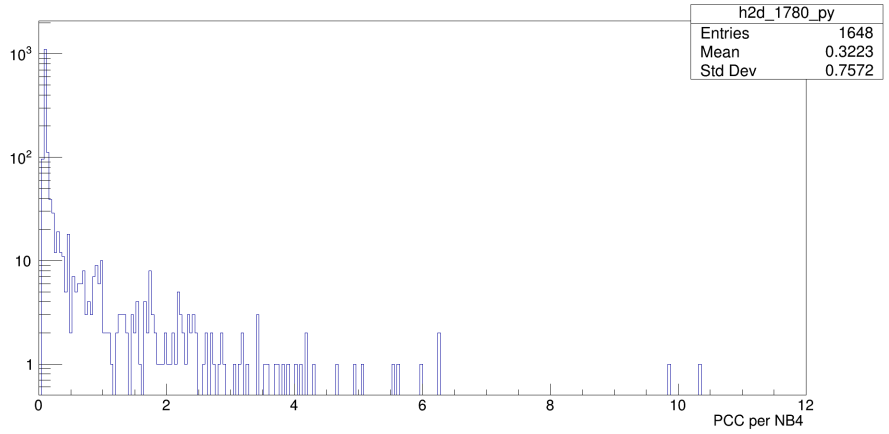

Fig. 4.4 PCC per NB4 profile for BCID 1780 from SS period I.

Table 4.1 Background mean value and SEM of each BCID for both SS periods .

SS period I		
BCID	**Mean**	**SEM**
265	0.3111	0.0172
865	0.2732	0.0135
1780	0.3223	0.0187
2192	0.2875	0.0159
3380	0.3157	0.0162

$\text{SSI}_{\text{Avg}} = \quad 0.302 \pm 0.0073$

SS period II		
BCID	**Mean**	**SEM**
265	0.3027	0.0148
865	0.297	0.0156
1780	0.304	0.0167
2192	0.2225	0.0114
3380	0.3064	0.0169

$\text{SSII}_{\text{Avg}} = \quad 0.287 \pm 0.0068$

Table 4.1 shows the mean en SEM values for each BCID for both SS periods and the average and error ($AvgErr = \sqrt{SEM_1^2 + SEM_2^2 + \cdots + SEM_N^2}/N$) per SS period. Having

both average values of SS, the average and error is taken, being this the value applied as a background correction: 0.29 ± 0.005.

4.5 Corrections

The PCC rates per NB4 are averaged per scan step (30s) and the uncertainty is calculated as the SEM. The following corrections are applied in the vdM FW:

1. Ghost and Satellite. Corrects for the presence of ghost and satellite spurious charges. This correction affects bunch currents. Satellite charges refers to charge in the colliding bunch crossing but not in the colliding RF bucket, while spurious charges refers to charge not in any nominally filled bunch slot.

2. Background. Value estimated above is subtracted to the rates.

3. Orbit drift. The Orbit Drift (OD) correction is composed of two independent corrections: separation correction and a rate correction. OD separation aims at correcting for the orbit drift in the scanning direction and only affects beam separation. OD rate aims at correcting for the orbit drift in the direction orthogonal to the scanning direction and only affects luminometer rate. The derived correction assumes that the beam overlap has a single gaussian shape. The correction reads the Σ in the orthogonal direction from the previous correction.

4. Beam Beam. Corrects Beam Beam deflection (BB) that happens during bunch crossings at the collision point. The deflection is calculated and added to the nominal separation.

5. Dynamic Beta. The so-called dynamic-$\beta*$ effect, which accounts for the fact that each beam has a defocusing effect on the other. This effect is calculated using reference beam transport simulations that are scaled to the beam energies, the β^* settings, and the measured intensities and convoluted beam widths.

6. Length Scale. It applies a linear scaling to the beam separation to convert it from the "CMS scale" to the actual "physics scale". This correction is estimated by analyzing pp collision vertices reconstruced by the CMS tracker.

7. Peak to peak. Corrects for error in peak calculation, when the scan does not cover the actual head-on collision of the beams.

4.6 van der Meer Scans and σ_{vis} Results

The measurements of PCC, beam separation and beam currents were plotted, fitted and corrected with the corrections described above. The fit model impleted is a guassian-like function:

$$Poly2G = P \cdot \left[1 + r_2 \cdot \left(\frac{x-\bar{x}}{\frac{\sigma}{1+r_2}}\right)^2\right] \cdot \exp\left[-\frac{1}{2}\left(\frac{x-\bar{x}}{\frac{\sigma}{1+r_2}}\right)^2\right]$$

where P is the peak value, $\bar{x}$ the mean, and σ (standard deviation) and r_2 are fit parameters. This model will be referred as "Poly2G". Fig. 4.5 shows the fitted graphs of the first vdM scan pair for BCID 1780. Fig. 4.6 shows the same graphs in logarithmic scale. Note that rates are normalized by the beam currents, which is a factor of eq. 3.6 $(R(0,0)/N_1N_2)$.

The rest of the BCIDs, vdM and imaging scans present a very similar behaviour. Fig 4.7 shows a plot of the chi2/ndof for all the seven scan pairs, having a mean value of 2.23. In all cases the fits converged. The $\Sigma_{x,y}$ (referred also as CapSigma) and peak values were extracted from the fits to compute σ_{vis}. Fig 4.8 shows $\Sigma_{x,y}$ and peak values for all scan pairs. As can be seen, both values reflects the fact that beam size increased over time in the x dimension and decreased over time in the y dimension.

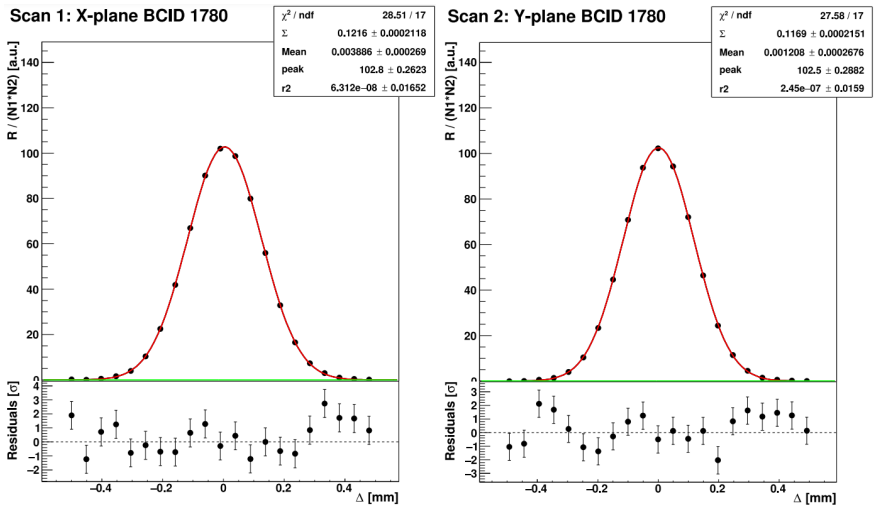

Fig. 4.5 Normalized rates and the resulting fitted curves with the Poly2G fit model (see text) as a function of the beam separation (Δ) for BCID 1780 for X (left) and Y (right) scan for the first vdM scan. Background subtraction and the corrections described in the previous section have been applied to the raw data before the fit.

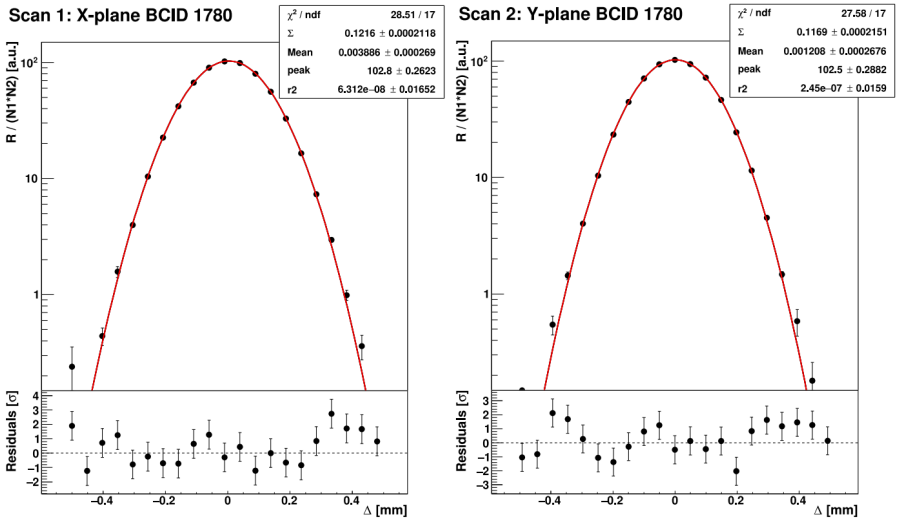

Fig. 4.6 Fig. 4.5 in logarithmic scale.

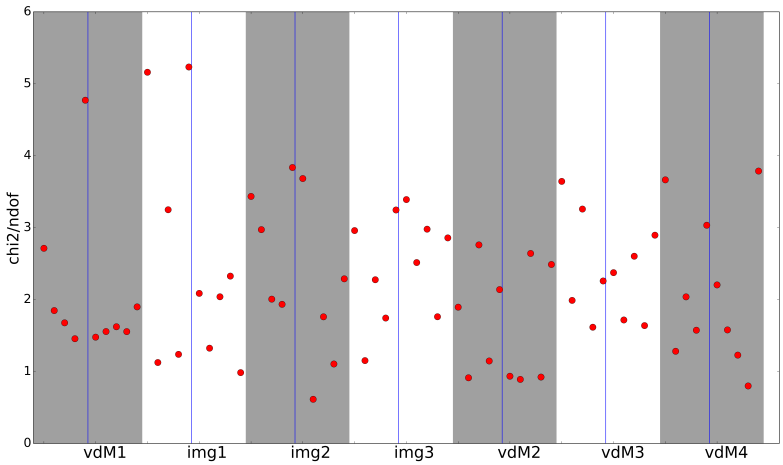

Fig. 4.7 chi2/ndof for all the scan pairs. Vertical blue lines divide the X (left) and Y (right) scans. In each scan, the BCIDs follow the same order: 265, 865, 1780, 2192, 3380.

The σ_{vis} of each BCID is computed from the fit results parameters showed in previous section ($\Sigma_{x,y}$ and peak) using 3.6 with $R(0,0) = (Peak_x + Peak_y)/2$; $Peak_{x,y}$ values are already normalized so 3.6 is rewritten as $\sigma = 2\pi\Sigma_x\Sigma_y(Peak_x + Peak_y)/2$.
Fig 4.9 shows σ_{vis} per BCID for all the scans. The error on σ_{vis} is assigned as $\sigma_{vis\mathrm{Err}} = 2\pi\sqrt{(\Sigma_y \cdot R \cdot \Sigma_{x\mathrm{Err}})^2 + (\Sigma_x \cdot R \cdot \Sigma_{y\mathrm{Err}})^2 + (\Sigma_x\Sigma_y R_{\mathrm{Err}})^2}$.
Fig 4.10 shows σ_{vis} per Scan, which corresponds to the weighted average of the five BCIDs

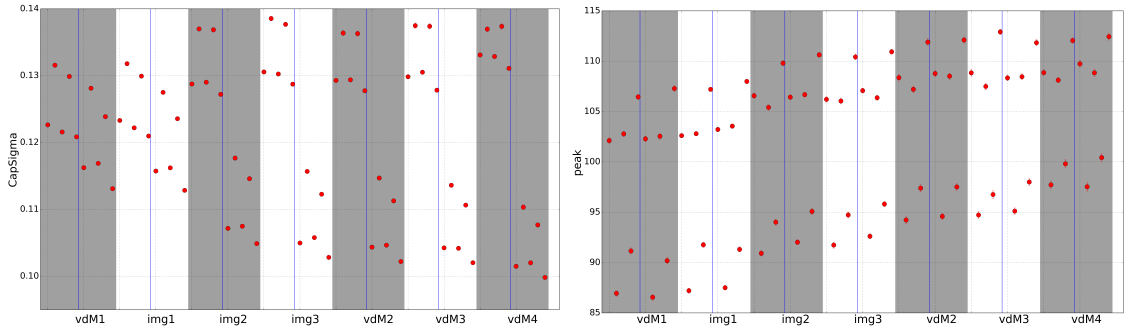

Fig. 4.8 Σ (left) and Peak values (right) extracted from the fitted graph to compute σ_{vis}. Vertical blue lines divide the X (left) and Y (right) scans. In each scan, the BCIDs follow the same order: 265, 865, 1780, 2192, 3380.

with the weight as $1/\sigma^2_{vis\text{Err}}$. The error is assigned as $1/\sqrt{\Sigma \frac{1}{\sigma^2_{vis\text{Err}}}}$.

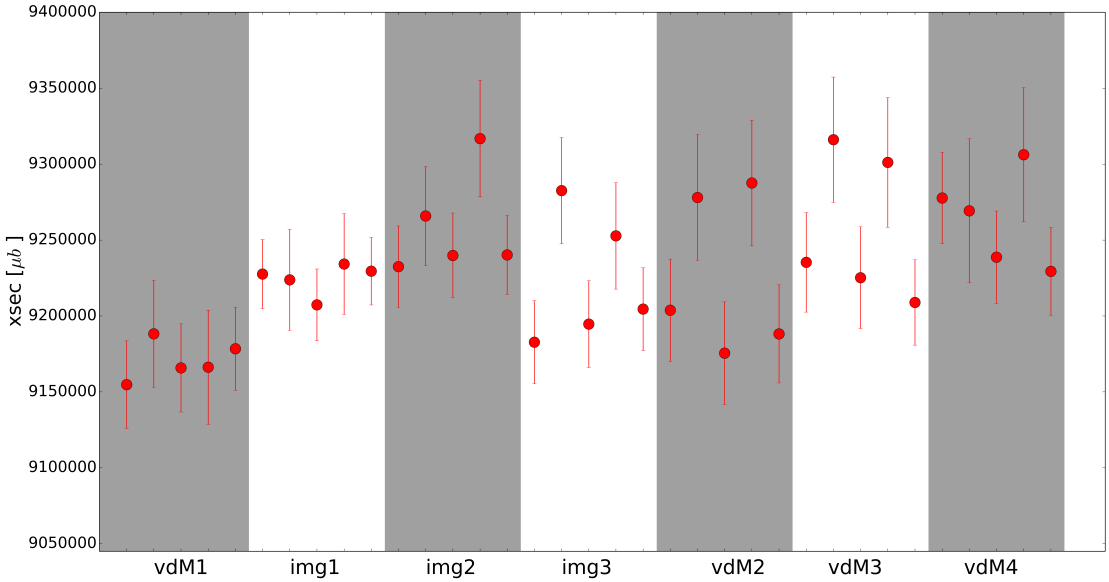

Fig. 4.9 σ_{vis} per BCID for all the scans. In each scan the BCIDs follow the same order: 265, 865, 1780, 2192, 3380.

The σ_{vis} per scan are averaged and assigning the error in the same way described above, giving a value of 9229 ± 8(stat.)mb.

As can be seen in Fig 4.10 (and Fig 4.9), there is some systematic variation in σ_{vis} from scan to scan, being the first vdM scan lower than the rest of the scans. The systematic error is assigned as $\sqrt{RMS^2 - stat^2}$.

Therefore the σ_{vis} value is

$$\sigma_{vis} = 9229 \pm 8(\text{stat.}) \pm 28(\text{syst.}) \text{ mb}. \tag{4.1}$$

This value is higher than the previously reported in ref. [18]: 5982 mb, which corresponds to a different selection of modules in the pixel detector. In the previous result, 1069 modules were removed, whereas the value of 9229 mb corresponds to 802 modules removed; the rate of pixel clusters is proportional to the number of modules.

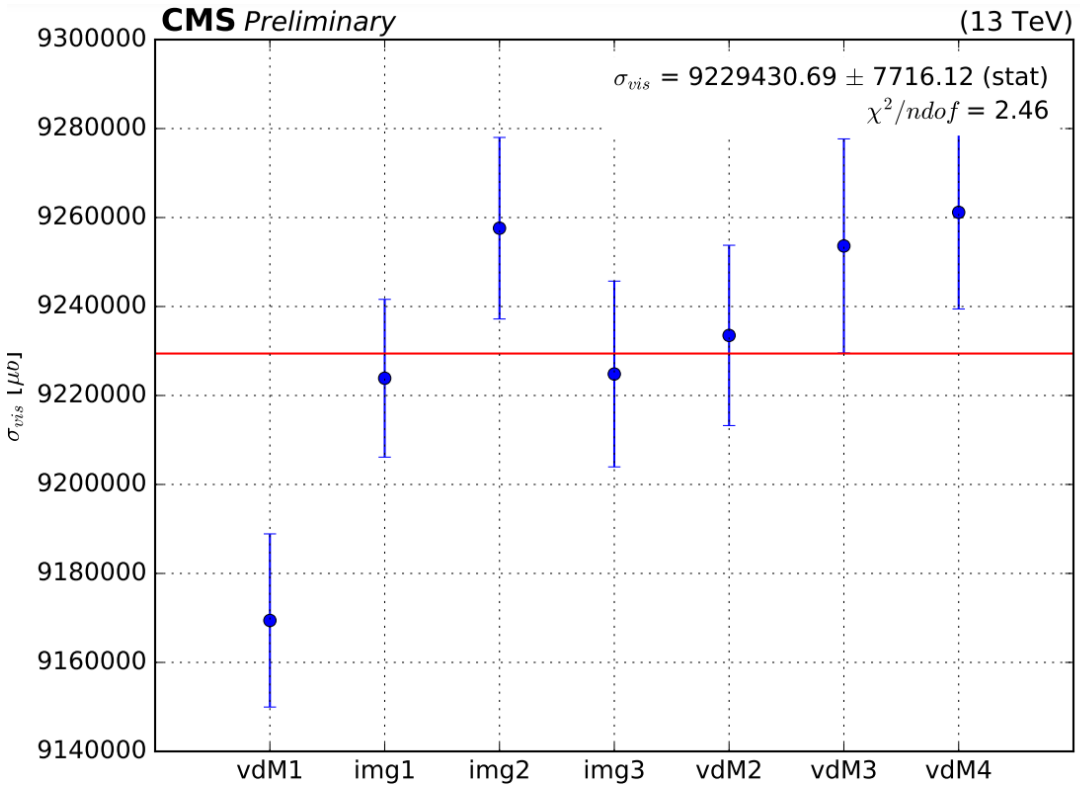

Fig. 4.10 σ_{vis} per scan.

Chapter 5

Summary and Outlook

This work focuses on the luminosity calibration for the PCC CMS luminometer from the van der Meer scans performed by the CMS Collaboration in summer 2018 for proton-proton collisions at $\sqrt{s} = 13$ TeV. Some aspects such as the luminosity and its importance, the CMS experiment, the PCC luminometer, and the calibration procedure to estimate σ_{vis} were covered.

A key part of this work was the reprocessing of the recorded data. One part of the reprocessing was applying a different selection of the Pixel detector modules, based on removing instabilities in luminosity measurement for the corresponding calibration period. The other part of the reprocessing concerns to the data process work flow, where a new step was added, exploiting the full statistics of the data, providing an improvement in the statistical uncertainty in the rates by a factor of 10, in the fit model and a better determination of the beam parameters, relative to the previous analysis reported. This new data implied the estimation of the background correction to the rates (PCC) from the two super separation periods, being this estimation also part of the analysis of this work.

To determine σ_{vis}, seven scan pairs (four standar vdM and three Imaging scans) were used. A systematic variation is observed from bunch to bunch and scan to scan, being the first vdM scan lower than the rest of the scans. The assinged value of the calibration is $\sigma_{vis} = 9229 \pm 8(stat.) \pm 28(syst.)$ mb.

The analysis and results reported in this work will be useful for an analysis of the precise luminosity measurement for Run2 in the CMS experiment of LHC, where the rest of the luminometers and its uncertainties will be studied (and improved).

References

[1] David J Griffiths. *Introduction to elementary particles; 2nd rev. version*. Physics textbook. Wiley, New York, NY, 2008. URL https://cds.cern.ch/record/111880. https://cds.cern.ch/record/111880.

[2] CMS Collaboration. Observation of a new boson at a mass of 125 GeV with the CMS experiment at the LHC. *Physics Letters B*, 716(1):30–61, 2012. doi: https://doi.org/10.1016/j.physletb.2012.08.021.

[3] ATLAS Collaboration. Observation of a new particle in the search for the Standard Model Higgs boson with the ATLAS detector at the LHC. *Physics Letters B*, 716(1): 1–29, 2012. doi: https://doi.org/10.1016/j.physletb.2012.08.020.

[4] Mark Thomson. *Modern Particle Physics*. Cambridge University Press, 2013. doi: 10.1017/CBO9781139525367.

[5] Alexander Belyaev and Douglas Ross. *Particle Accelerators*, pages 201–219. Springer International Publishing, Cham, 2021. doi: 10.1007/978-3-030-80116-8_13.

[6] Stephen Myers and Herwig Schopper. *Particle Physics Reference Library Volume 3: Accelerators and Colliders.* 01 2020. doi: 10.1007/978-3-030-34245-6.

[7] P. Grafström and W. Kozanecki. Luminosity determination at proton colliders. *Progress in Particle and Nuclear Physics*, 81:97–148, 2015. doi: https://doi.org/10.1016/j.ppnp.2014.11.002.

[8] M.L. Mangano, Motivations and precision targets for an accurate luminosity determination at the LHC, *CERN-Proceedings-2011-011*, https://cds.cern.ch/record/1347440.

[9] Lyndon Evans and Philip Bryant. LHC machine. *Journal of Instrumentation*, 3(08): S08001–S08001, Aug 2008. doi: 10.1088/1748-0221/3/08/s08001.

[10] CMS Collaboration. The CMS experiment at the CERN LHC. *Journal of Instrumentation*, 3(08):S08004–S08004, Aug 2008. doi: 10.1088/1748-0221/3/08/s08004.

[11] ATLAS Collaboration. The ATLAS experiment at the CERN large hadron collider. *Journal of Instrumentation*, 3(08):S08003–S08003, Aug 2008. doi: 10.1088/1748-0221/3/08/s08003.

[12] ALICE Collaboration. The ALICE experiment at the CERN LHC. *Journal of Instrumentation*, 3(08):S08002–S08002, Aug 2008. doi: 10.1088/1748-0221/3/08/s08002.

[13] The LHCb Collaboration. The LHCb detector at the LHC. *Journal of Instrumentation*, 3(08):S08005–S08005, Aug 2008. doi: 10.1088/1748-0221/3/08/s08005.

[14] Eva Halkiadakis. Introduction to the LHC Experiments. In *Theoretical Advanced Study Institute in Elementary Particle Physics: Physics of the Large and the Small*, pages 489–518, 2011. doi: 10.1142/9789814327183_0009.

[15] Mike Lamont. Status of the LHC. *Journal of Physics: Conference Series*, 455: 012001, Aug 2013. doi: 10.1088/1742-6596/455/1/012001.

[16] CMS Collaboration. Precision luminosity measurement in proton-proton collisions at $\sqrt{s}$ = 13 tev in 2015 and 2016 at cms. *The European physical journal. C, Particles and fields*, 81:800, 01 2021. doi: 10.1140/epjc/s10052-021-09538-2.

[17] CMS luminosity measurement for the 2017 data-taking period at $\sqrt{s} = 13$ TeV. Technical report, CERN, Geneva, 2018. URL https://cds.cern.ch/record/2621960.

[18] CMS luminosity measurement for the 2018 data-taking period at $\sqrt{s} = 13$ TeV. Technical report, CERN, Geneva, 2019. URL https://cds.cern.ch/record/2676164.

[19] CMSPublic Web. CMS Luminosity - Public Results. Delivered luminosity versus time for 2010-2012 and 2015-2018 (pp data only), 2022. URL https://twiki.cern.ch/twiki/bin/view/CMSPublic/LumiPublicResults. [Online; accessed September 23, 2022].

[20] A.M. Sirunyan et al. Particle-flow reconstruction and global event description with the CMS detector. *Journal of Instrumentation*, 12(10):P10003–P10003, Oct< 2017. doi: 10.1088/1748-0221/12/10/p10003.

[21] Brian R Martin and Graham Shaw. *Particle Physics*. Manchester Physics Series. John Wiley & Sons, Nashville, TN, 4 edition, January 2017.

[22] W. Adam et al. The CMS phase-1 pixel detector upgrade. *Journal of Instrumentation*, 16(02):P02027–P02027, Feb 2021. doi: 10.1088/1748-0221/16/02/p02027.

[23] The CMS Collaboration. Description and performance of track and primary-vertex reconstruction with the CMS tracker. *Journal of Instrumentation*, 9(10):P10009–P10009, Oct 2014. doi: 10.1088/1748-0221/9/10/p10009.

[24] S van der Meer. Calibration of the effective beam height in the ISR. Technical report, CERN, Geneva, 1968. URL https://cds.cern.ch/record/296752.

[25] CMS Luminosity Based on Pixel Cluster Counting - Summer 2013 Update. Technical report, CERN, Geneva, 2013. URL https://cds.cern.ch/record/1598864.

[26] CMS Luminosity Based on Pixel Cluster Counting - Summer 2012 Update. Technical report, CERN, Geneva, 2012. URL https://cds.cern.ch/record/1482193.

[27] CMS luminosity measurement for the 2015 data-taking period. Technical report, CERN, Geneva, 2017. URL https://cds.cern.ch/record/2138682.

[28] Olena Karacheban. Performance of the BRIL luminometers at CMS in Run 2. *PoS*, EPS-HEP2019:194, 2020. doi: 10.22323/1.364.0194.

[29] S. Müller. Simulation of beam-induced backgrounds in comparison with data from the CMS pixel and other inner radii detectors. *Nuclear Instruments and Methods in Physics Research Section A: Accelerators, Spectrometers, Detectors and Associated Equipment*, 650(1):33–36, 2011. doi: https://doi.org/10.1016/j.nima.2010.11.082. International Workshop on Semiconductor Pixel Detectors for Particles and Imaging 2010.